Experimental and theoretical study of cross-phase modulation in InGaAs/AlAsSb coupled double quantum wells with a AlGaAs coupling barrier

G. W. Cong,* R. Akimoto,† K. Akita, S. Gozu, T. Mozume, T. Hasama, and H. Ishikawa
Network Photonics Research Center, National Institute of Advanced Industrial Science and Technology (AIST), AIST Tsukuba Central 2-1, Umezono 1-1-1, Tsukuba, Ibaraki 305-8568, Japan
(Received 30 April 2009; published 10 July 2009)

Our experiment revealed that the cross-phase modulation (XPM) power efficiency was enhanced by decreasing the doping density in InGaAs/AlAsSb coupled double quantum well (CDQW) waveguides with an AlGaAs coupling barrier. To interpret this enhancement and systematically study the physics of XPM, we implemented the eight-band $k \cdot p$ calculation based on the interband dispersion model under intersubband excitation [proposed by our group in Phys. Rev. B **75**, 075308 (2008) for XPM]. This calculation allows for an evaluation of the contributions to XPM, not only from the lowest interband transition (HH1-e1), but also from higher transitions (LH1-e1, HH2-e2). By considering all of these contributions, the calculated carrier density dependence of the index change well explains the enhancement in XPM efficiency, which mainly results from the redshift of the interband absorption edge when the doping density is decreased. To further enhance the XPM efficiency, we decreased the Al composition in the coupling barrier in order to lower the interband absorption edges for both HH1-e1 and LH1-e1. We predicted that the XPM efficiency would be tripled by decreasing the Al composition from 0.5 to zero for a carrier density of $\sim 1 \times 10^{18}$ cm^{-3}.

DOI: 10.1103/PhysRevB.80.035306 PACS number(s): 78.67.De, 42.50.Ct, 73.21.Fg

I. INTRODUCTION

Modulating the phase of light plays important roles in optical signal processing, and the growth in bit rates requires continuous modulation rate enhancements.[1] It is well known that the intersubband transition (ISBT) in semiconductor quantum wells (QWs) has an ultrafast relaxation time that satisfies the high-speed requirement.[2] Recently, we discovered a new all-optical cross-phase modulation (XPM) in InGaAs/AlAsSb coupled double quantum wells (CDQWs) that has a picosecond characteristic time.[3] This XPM enables us to set up interferometer-type all-optical switches for high-speed telecommunication.[3–5] We have clarified the physical mechanism behind this XPM, which originates from the interband dispersion under intersubband excitation.[6] When the TM light excites intersubband excitation, carriers at the ground state are pumped to a high-energy subband. The carrier reduction in the ground state shifts the quasi-Fermi-level downward. Such a downshift induces an interband absorption $\Delta\alpha$, which occurs at wavevectors near the Fermi level. $\Delta\alpha$ has a corresponding index change (Δn) dispersion due to their common origins in susceptibility.[7] It is this index change that produces a phase shift ($\Delta\phi = 2\pi L \Delta n/\lambda$, L is the length over which Δn is effective) for TE probe light. This interband dispersion model has the important feature that the index change increases when the probe photon energy is tuned to the interband absorption edge.[6]

As known, the interband absorption edge strongly depends on the in-plane band dispersions and doping level.[8] Unfortunately, the model we proposed in Ref. 6 neglects the band dispersions and approximately treats the induced interband absorption as a Lorentz function after introducing several fitting parameters. Moreover, the induced interband absorption has several allowed transitions due to the valence-band subbands, such as the HH and LH bands, as does the index change. Therefore, we can no longer use a simple Lorentz function to describe the induced absorption because each transition has its own absorption edge. How much each component contributes and how such contributions vary with different CDQW structures should be clarified in order to optimize the CDQW design and allow us to achieve a large XPM using minimal power. This clearly involves the calculation of the interband absorption spectrum since the induced absorption $\Delta\alpha$ can be understood as the difference between two interband absorption spectra under electron densities N and N-ΔN, i.e., $\Delta\alpha = \alpha[E_f(N-\Delta N)] - \alpha[E_f(N)]$, where ΔN is the electron density change due to intersubband excitation and E_f is the quasi-Fermi-level. Calculating the electron density dependent interband absorption spectrum requires the in-plane conduction-band and valence-band dispersions. This requirement is obviously beyond our work in Ref. 6 which could not quantitatively evaluate the index change for different CDQWs and doping densities. Therefore, in this study we carried out doping density dependent experiments and an eight-band $k \cdot p$ calculation to explain the experiments, which gave a complete physical picture for XPM.

In this study, we first experimentally obtained the doping density dependence of XPM efficiency. Thereafter, we calculated the interband dispersion model under intersubband excitation through the eight-band $k \cdot p$ method and quantitatively evaluated the index change for different doping densities and CDQWs. The calculated results agreed well with the experiment. This paper is organized as follows. The experimental details and results are given in Sec. II. Section III presents the details of our $k \cdot p$ calculation. In Sec. IV, we show the comparison between the calculated interband absorption spectrum and the experimental one and discuss the evolution of the interband absorption, induced interband absorption, and index change with an increase in electron density. Section V shows how the CDQW structure was optimized to enhance the XPM efficiency and we summarize our findings in Sec. VI.

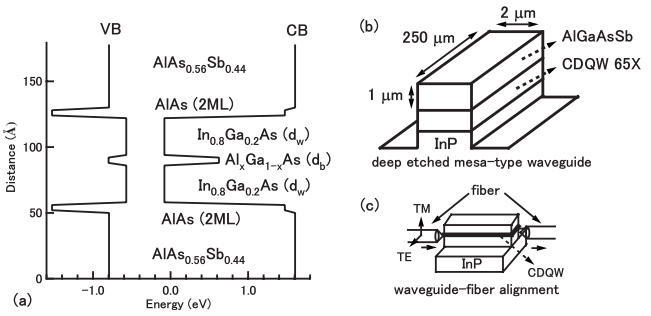

FIG. 1. (a) CDQW structure with AlGaAs as the coupling barrier. CB: conduction band. VB: valence band. (b) Mesa waveguide (WG) structure. (c) A fiber-based waveguide measurement scheme using waveguide-fiber alignment for measuring waveguide insertion loss and phase shift.

II. EXPERIMENTS

A. Merits of AlGaAs coupling barrier

A CDQW with an AlGaAs coupling barrier has recently been proven to have a much larger XPM efficiency (~0.5 rad/pJ) (Ref. 9) than the previous AlAs (~0.0305 rad/pJ) (Ref. 4) and InAlAs coupling barriers (~0.15 rad/pJ).[10] This improvement can be explained by the interband dispersion model since the interband absorption edge measured by a Fourier transform infrared spectrometer (FTIR) is obviously shifted toward the low energy side for an AlGaAs barrier compared to an AlAs one.[9] A decrease in the energy separation between the absorption edge and probe photon energy of ~0.8 eV enhances the XPM efficiency. Therefore, we adopted the AlGaAs coupling barrier based on the following considerations from the interband dispersion model: (1) AlGaAs has a smaller conduction-band offset (CBO) and valence-band offset (VBO) with respect to InGaAs than AlAs, which was expected to decrease the carrier confinement in the conduction band and valence band. This will lower the interband absorption edge close to 0.8 eV, which is generally the target photon energy for telecommunication. (2) Compared to InAlAs, because of the close lattice constants between GaAs and AlAs, AlGaAs almost maintains the constant tensile strain state over the whole composition range. This allows the adjustment of band offsets in a larger scope, and also maintains the stability of the strain condition. More importantly, the tensile strain in AlGaAs further elevates the LH potential in the coupling barrier so that the confinement of LH in the well is weakened, which as a result will shift the LH bands upward and enhance the contribution from LH. Therefore, it is necessary to systematically study this promising CDQW with an AlGaAs coupling barrier from both the experimental and calculation sides in order to further optimize this system.

B. Sample details and measurement system

Figure 1(a) shows the band profile of an InGaAs/AlAsSb CDQW using AlGaAs as the coupling barrier. The well thickness d_w, coupling barrier thickness d_b, and Al composition x are adjustable parameters. We used three groups of waveguide samples and an undoped epilayer sample, all of which were grown on InP substrates by molecular-beam epitaxy. The AlAsSb barrier was in a latticed matched condition, while the InGaAs well was compressively strained. For the waveguide samples, the well was doped by silicon. Groups 1 (d_w=3 nm, d_b=2 ML, x=0.5) and 2 (d_w=2.9 nm, d_b=3 ML, x=0.5) both showed the intersubband transition e1-e4 at around 1.55 μm, but they had very different interband absorption edges. Thus, they were anticipated to exhibit different XPM efficiencies. For 1 and 2, 2-ML-AlAs interface layers were inserted between the well and AlAsSb barrier layers to balance the strain in the well. Groups 1 and 2 each had three samples of different doping densities. The intended range of electron density N was $2.5 \sim 6 \times 10^{18}$ cm^{-3}. The samples in group 3 were previously grown samples with AlAs coupling barriers, which were selected for comparison with groups 1 and 2. These old samples did not have AlAs interfaces between the InGaAs well and AlAsSb barrier. Three groups of samples were fabricated into 250-μm-long and 2-μm-wide deep etched mesa structures by standard processing techniques, as shown in Fig. 1(b). All waveguide samples had a 1 μm AlGaAsSb upper cladding layer. The undoped epilayer sample without a cladding layer adopted the same CDQW structure as group 1 and was backside polished to measure the interband absorption spectrum of TE polarization by FTIR under normal incidence. The details for the samples in group 1 and the epilayer sample can be found in Ref. 9. The sample parameters are summarized in Table I.

For measuring phase shift and waveguide insertion loss, we adopted waveguide-fiber alignment scheme in Fig. 1(c) where the light propagates in the CDQW plane and can be adjusted to either TE or TM polarization. Figure 2(a) shows the setup for the fiber-based XPM measurement system, which was slightly different from the previous one.[3,6] In order to convert phase modulation to intensity variation, the interferometer in our previous setup was constructed using a

TABLE I. Quantum well parameters.

Group	No. 1			No. 2			No. 3		
Sample number	644	645	646	647	648	649	5122	5155	1777
d_w (nm)	3	3	3	2.9	2.9	2.9	2.5	2.65	2.6
d_b (ML)	2	2	2	3	3	3	3	2	4
Al_x	0.5	0.5	0.5	0.5	0.5	0.5	1	1	1
Doping density (1×10^{18}/cm^3)	6	2.5	4.5	4.5	6	2.5	2–2.5	2–2.5	14

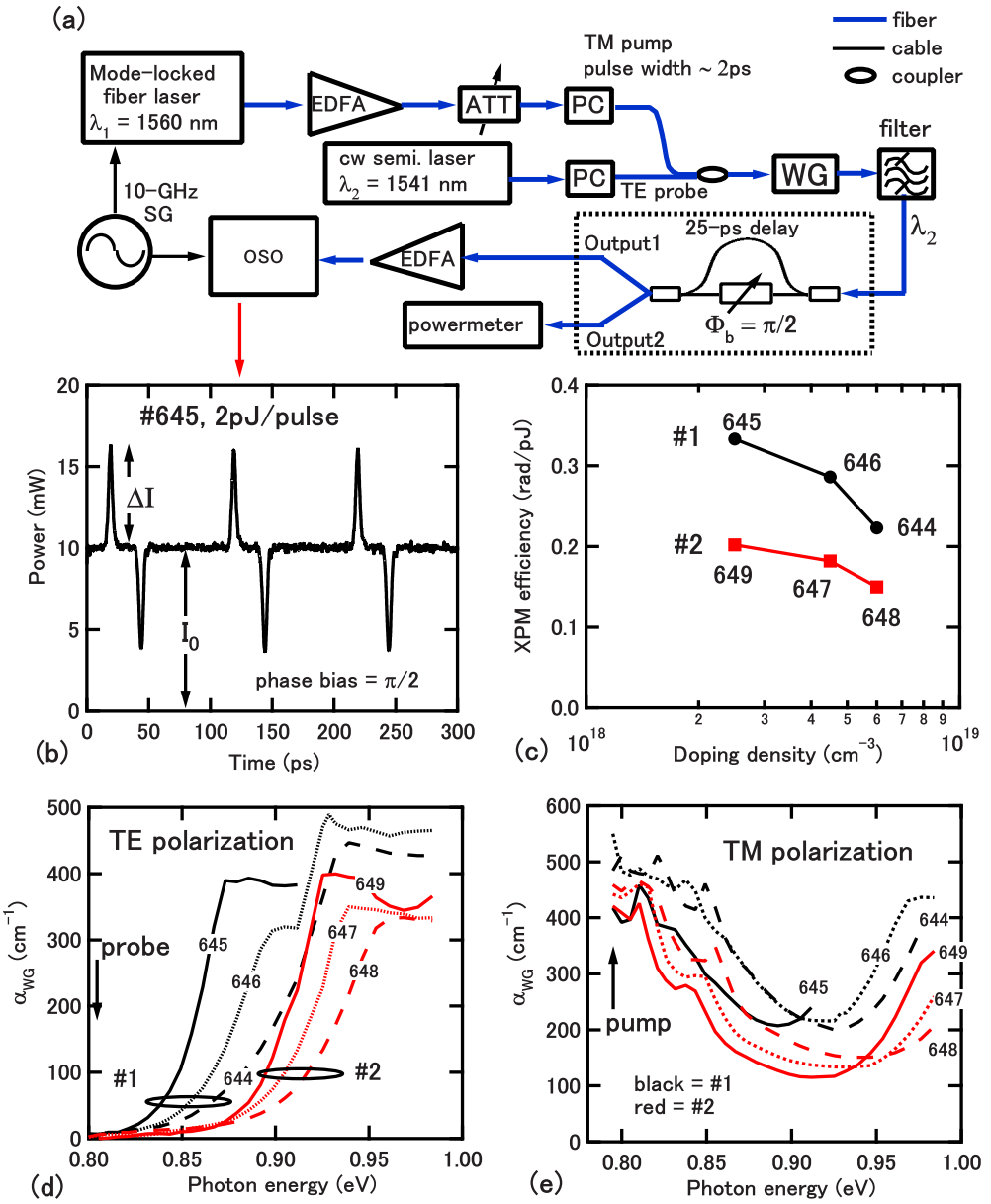

FIG. 2. (Color online) (a) Fiber-based XPM measurement system. WG: waveguide, OSO: optical sampling oscilloscope, phase bias $\Phi_b = \pi/2$. The TM pump laser was a 10 GHz mode-lock fiber laser at $\lambda_1 = 1560$ nm and a cw semiconductor laser at $\lambda_2 = 1541$ nm was used as a probe. (b) An intensity waveform recorded by OSO at a 2 pJ/pulse for No. 645. (c) Measured XPM efficiency as a function of doping density. (d) and (e) show the waveguide absorption coefficients for TE and TM polarizations obtained from waveguide insertion losses, respectively. The pump and probe wavelengths are indicated in (d) and (e).

differential group delay, a prepolarization controller, a post polarization controller, and a post polarizer; however, the current setup in Fig. 2(a) was constructed using a compact delay-line interferometer. This interferometer had in-phase and out-of-phase ports and the phase bias Φ_b could be set to $\pi/2$ by simply monitoring the power in one port, while the other was connected to an optical sampling oscilloscope (OSO) through an erbium-doped fiber amplifier (EDFA). A mode-locked fiber laser operated at 1560 nm generated 2 ps wide 10 GHz pulses as the TM pump light to excite intersubband transition, and a semiconductor laser generated the continuous wave at 1541 nm as the TE probe light.

C. XPM efficiency and WG absorption

The time-domain method of measuring the phase shift by utilizing an OSO was introduced in Refs. 3 and 4. Figure 2(b) shows a typical intensity variation waveform recorded by an OSO for No. 645 at a 2 pJ pulse energy, which showed the largest XPM efficiency. The pump-induced phase shift resulted in constructive and destructive interferences with a 25 ps time difference, as presented by the periodic positive and negative peaks with a reference at the middle average power. The measured XPM efficiencies are given as a function of the doping density for groups 1 and 2 in Fig. 2(c). For a given doping density, 1 had a larger XPM efficiency than 2,

and a decrease in XPM efficiency was seen in both groups when the doping density was increased. Considering the important feature of the interband dispersion model under intersubband excitation that the index change increases when the absorption edge is tuned to the photon energy of the probe light,[6] both TE and TM insertion losses were measured using a waveguide-fiber alignment setup[6] shown in Fig. 1(c) to examine the interband absorption edge. The insertion losses were converted to waveguide absorption coefficients α_{WG} by using the waveguide length (250 μm). Therefore, we can obtain the waveguide absorption spectra for TE and TM polarization, as shown in Figs. 2(d) and 2(e), respectively. For a 250 μm length, $\alpha_{WG}=500$ cm^{-1} means a >54 dB loss. However, this >50 dB insertion loss could not be correctly measured due to the transmission limitations of the optical components, such as the polarization controller. These measurement limitations yielded a steplike absorption in Fig. 2(d).

The interband absorption accounts for the loss of TE light. As shown in Fig. 2(d), the absorption edges for both groups shifted to a higher energy with increasing the doping density due to the carrier filling in the conduction band, and a higher doping density induced a slower increase speed of the absorption with an increase in the photon energy. For equally doped samples, No. 2 had a larger absorption edge energy than No. 1. Combined with Fig. 2(c), it is clear that a larger energy difference between the interband absorption edge and the probe photon energy ($\sim$0.8 eV) results in a smaller XPM efficiency. This well supports our model.[6] For example, No. 649 is larger than No. 645 by $\sim$50 meV in the absorption edge; thus the XPM efficiency of No. 649 is only 60% of No. 645.

The TM absorption has two origins: intersubband absorption and interband absorption. FTIR (not shown) showed that the absorption peak of the intersubband transition e1–e4 was located at around 1.55 μm for both groups 1 and 2. Consequently, we observed an absorption band at around 0.8 eV, as seen in Fig. 2(e). When the photon energy increased, the intersubband absorption gradually weakened, while the interband absorption was enhanced since the photon energy approached the interband absorption edge of the TM polarization and moved away from the e1–e4 transition energy. Therefore, a minimum absorption can be seen in Fig. 2(e). The TM interband absorption edge also had a clear doping density dependence, shifting to a higher energy when the doping density increased. For each sample, the TM interband absorption edge was higher than the TE one because the TE and TM interband absorptions resulted from HH- and LH-like bands (LH-e1 $>$ HH-e1), respectively.

Based on the experimental results discussed above, we can reach the conclusion that the XPM efficiency decreases due to a blueshift in the interband absorption edge when the doping density is increased. This conclusion can be qualitatively understood by our model.[6] However, this model cannot quantitatively interpret such a doping density dependence and the difference in absorption edges between 1 and 2. Therefore, we implemented $k\cdot p$ calculation to explain the above experimental results because $k\cdot p$ calculation allowed us to evaluate the doping density dependent interband absorption.

III. MODEL BASED ON $k\cdot p$ CALCULATION

A. $k\cdot p$ calculation and parameters

To make it easier to describe the comparison between the experiment and calculation, we first define the calculated CDQW structures in this paper. The calculated groups 1 ($d_w=3$ nm, $d_b=2$ ML, $x=0.5$) and 2 ($d_w=2.9$ nm, $d_b=3$ ML, $x=0.5$) were structurally the same as the experimentally designed ones. For group 3 in the calculation, we introduce No. 3–1 ($d_w=2.6$ nm, $d_b=2$ ML, $x=1$) and No. 3–2 ($d_w=2.6$ nm, $d_b=4$ ML, $x=1$), which differ only in the barrier thickness.

The $k\cdot p$ calculation in this study followed Bahder's paper[11] with the inclusion of the strain effect. The 8×8 Hamiltonian matrix and strain interaction matrix were written into differential equations based on the parameter discretization of the quantum well.[12] Then an $8M\times 8M$ complex matrix (M is the discretization number along the growth direction) was diagonalized to obtain eigenvalues and eigenstates. Axial approximation was adopted so that the energy subbands were isotropic in the wave vector plane and the biaxial strain was considered. Using the complex eigenstates, we could calculate the in-plane wave vector ($k_{\|}$) dependent dipole matrix element for both TE and TM polarizations.[13] To calculate the interband absorption spectrum, three further steps were taken: (1) for a given electron density, the Fermi level was self-consistently determined using the CB density of states (DOS) ($\Sigma N_i(E_f)=N$, i: subband index in CB); (2) the joint DOS for interband transitions was calculated from the band dispersions; and (3) the interband absorption spectrum was calculated by energetically integrating the product of the joint DOS, difference in electron occupation probability between the CB and VB subbands, dipole matrix element, and a Lorentz-type absorption with an interband dephasing time=400 fs.[8] In this study, all calculated interband absorption spectra are under TE polarization because the phase shift happens for TE probe light in our experiments. If the intersubband excitation decreased the electron density by ΔN, the induced interband absorption $\Delta\alpha$ equaled $\alpha(N\text{-}\Delta N)\text{-}\alpha(N)$. In the spectral calculation, the quasithermal equilibrium was assumed since the pump pulse width (2 ps) was much larger than the intersubband dephasing time ($\sim$300 fs).[14] Consequently, the index dispersion was obtained from the induced absorption by the Kramers-Kronig transform.

It is necessary to comment on the parameters used in the $k\cdot p$ calculation. The CBO of $AlAs_{0.56}Sb_{0.44}$ with respect to $In_{0.53}Ga_{0.47}As$ is widely accepted to be about 1.6 eV, since this value works well in predicting subbands in $In_{0.53}Ga_{0.47}As/AlAs_{0.56}Sb_{0.44}$ quantum cascade lasers[15] and quantum wells.[16] Using $E_g=2.39$ eV for $AlAs_{0.56}Sb_{0.44}$, several interband transition energies in the photoreflection spectra were well predicted by a calculation based on the effective-mass model for a 10 nm-wide $In_{0.53}Ga_{0.47}As/AlAs_{0.56}Sb_{0.44}$ single QW.[17] In our calculation, we used $E_g=2.4$ eV for $AlAs_{0.56}Sb_{0.44}$ and the CBOs for $AlAs_{0.56}Sb_{0.44}$ and AlAs with respect to $In_{0.8}Ga_{0.2}As$ were 1.7 and 1.6 eV, respectively. In fact, the variation in E_g of $AlAs_{0.56}Sb_{0.44}$ from 2.4 to 2.5 eV when fixing its CBO =1.7 eV had little influence on the lowest three VB sub-

bands, because the AlAs interfaces had a much larger VBO than $AlAs_{0.56}Sb_{0.44}$. The VB deformation potentials for $In_{0.8}Ga_{0.2}As$ were taken from Ref. 18 because the calculation in this paper agreed well with their experiment. The other parameters were all from Ref. 19, and linear interpolation was used to determine parameters for the ternary alloys if the bowing parameters were unknown. The temperature was set to be 300 K. Table II summarizes the parameters.

B. Model refined by $k \cdot p$ calculation

Figure 3(a) shows the calculated band dispersion curves, which are used to refine the interband dispersion model under intersubband excitation proposed in our previous work.[6] When the intersubband excitation pumps electrons from the ground state e1 to the excited state e4, the Fermi level E_f undergoes a downshift, which induces several allowable interband absorptions, such as HH1-e1 and LH1-e1 (dashed arrows). Each of these induced absorptions has a corresponding index dispersion due to the origins of the absorption and index in susceptibility.[7] The total index dispersion is the sum of the contributions from all of the induced absorptions. The induced absorption at the nonzero in-plane wave vector $k_{\|}$ also includes transitions, such as HH2-e1 and HH1-e2, that are originally inhibited at $k_{\|}=0$, because the selection rule is broken due to band mixing. Such band mixing features band anticrossings, which can be found at about $k_{\|}=0.03$ 1/Å between HH1 and HH2 and at $k_{\|}=0.04$ 1/Å between LH1 and HH3, as seen in Fig. 3(a). These two band anticrossings are more clearly observed in Fig. 3(b), where the transition dipole matrix elements of HH1-e1 and HH2-e1 exhibit contrary evolution with $k_{\|}$, as do those of HH1-e2 and HH2-e2, and those of LH1-e1 and HH3-e1.

Figure 3(b) also shows the Fermi wavevector (k_{Ef}) for several electron densities to track the variation in the interband absorption edge and dipole moment matrix with electron density. We can consider the sums of dipole moment matrices HH1-e1+HH2-e1 and HH1-e2+HH2-e2 because of the band mixing between HH1 and HH2. These two sums and the LH1-e1 dipole moment matrix all decrease with an increase in $k_{\|}$. The increase in $k_{\|}$ also corresponds to increases in the transition energies HH1-e1, HH2-e1, and LH1-e1, which can be clearly observed from the band curves in Fig. 3(a). When the electron density increases, E_f shifts upward so that k_{Ef} increases, as shown by the arrows in Fig. 3(b). Then the absorption edge will undergo blueshift and the dipole moment matrix will decrease for transitions to e1. Therefore, XPM should have an obvious dependence on the doping density. This refined model based on the $k \cdot p$ method enables us to evaluate such dependence with all of the allowable interband transitions considered.

IV. INTERBAND ABSORPTION AND XPM

A. Comparison between the calculated and experimental spectra

The interband absorption spectrum of TE polarization can be measured by FTIR under normal incidence for the backside polished undoped epilayer sample since the light propa-

TABLE II. Parameters used in $k \cdot p$ calculation. Band gap E_g, lattice constant a, Luttinger parameters γ_1, γ_2, and γ_3, spin-orbit-splitting energy Δ_{so}, elastic constants C_{11} and C_{12}, conduction-band deformation potential a_c, valence-band deformation potential a_v, and shear deformation potential b. l.i. stands for linear interpolation.

	GaAs	InAs	AlAs	AlSb	$In_xGa_{1-x}As$	$Al_xGa_{1-x}As$	$AlAs_xSb_{1-x}$
$E_g(T=300\ \mathrm{K})$/eV	1.423	0.353	3	2.3	$0.353x+1.423(1-x)-0.477x(1-x)$	$1.424+1.155x+0.37x^2$	$2.4(x=0.56)$
a(A)	5.6533	6.0584	5.6611	6.1355	l.i.	l.i.	l.i.
γ_1	6.98	20.0	3.76	5.18	l.i.	l.i.	l.i.
γ_2	2.06	8.5	0.82	1.19	l.i.	l.i.	l.i.
γ_3	2.93	9.2	1.42	1.97	l.i.	l.i.	l.i.
Δ_{so}/eV	0.34	0.39	0.275	0.676	$0.39x+0.34(1-x)-0.15x(1-x)$	l.i.	$0.275x+0.676(1-x)-0.15x(1-x)$
$C_{11}/10^{11}$ Pa	12.21	8.33	12.5	8.769	$[8.33xa_{InAs}+12.21(1-x)a_{GaAs}]/a_{InGaAs}$	l.i.	l.i.
$C_{12}/10^{11}$ Pa	5.66	4.53	5.34	4.34	$[4.53xa_{InAs}+5.66(1-x)a_{GaAs}]/a_{InGaAs}$	l.i.	l.i.
a_c/eV	−7.17	−5.08	−5.64	−4.5	$-5.08x-7.17(1-x)-2.61x(1-x)$	l.i.	l.i.
a_v/eV	−8.46	−6	−2.47	−1.4	l.i.	l.i.	l.i.
b/eV	−1.7	−1.8	−2.3	−1.35	l.i.	l.i.	l.i.

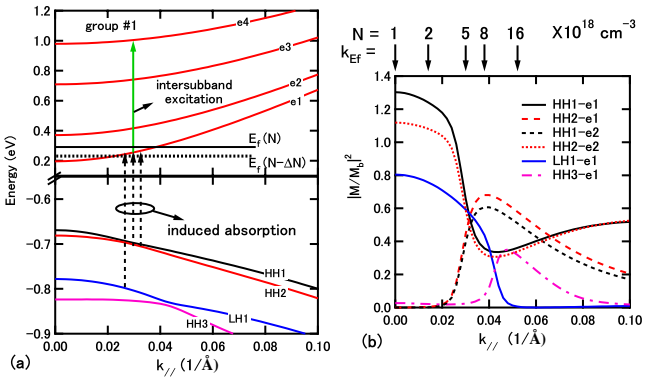

FIG. 3. (Color online) (a) Calculated in-plane dispersions of the lowest four CB and highest four VB subbands for group 1 (d_w=3 nm, d_b=2 ML, and Al_x=0.5). The induced interband transition (dashed arrows) by intersubband excitation (green arrow) is shown. (b) Dipole matrix elements versus in-plane wavevector $k_{||}$ for TE polarization. The Fermi wave vectors k_{Ef} are indicated for several electron densities by black arrows at the top. M_b is the bulk transition matrix element.

gates along the normal direction of CDQW plane. Therefore, we can compare the measured interband absorption spectrum with the calculated one for the undoped sample of group 1, as shown in Fig. 4(a), where both spectra are normalized to the well thickness. The calculated one well predicts: (1) three absorption steps (HH1-e1, LH1-e1, and HH2-e2), (2) the transition energies of HH1-e1 and LH1-e1, and (3) the absorption strength ratio between LH1-e1 and HH1-e1. These three points prove the correctness of the calculated band dispersions and dipole matrix element. It should be mentioned that the absorption strength enhancement at the absorption edge in the experimental spectra may come from an excitonic effect that was not included in our calculation. The excitonic effect could be left out of consideration because such an effect disappeared in our doped samples.[9] Therefore, the calculated spectra were effective for comparing the doped QW structures with regard to evaluating XPM efficiency.

B. Components of α, $\Delta\alpha$, and Δn

Taking group 1 as an example, we show the components of the interband absorption spectrum α at the electron density $N=1\times10^{18}$ cm^{-3} in Fig. 4(b). Groups 2 and 3 have similar components except for the differences in transition energies. The lowest two sublevels, e1 and e2, in CB and three sublevels (HH1, HH2, and LH1) in VB were considered in the absorption spectrum calculation. In Fig. 4(b), the interband absorption edge is dominated by HH1-e1, and the second and third absorption steps from low energy to higher originate from LH1-e1 and HH2-e2, respectively. The evolutions of the absorption magnitude with photon energy are determined by the dipole matrix elements, as shown in Fig. 3(b). The band anticrossing we introduced in Sec. III B explains why HH1-e1 starts to decrease when HH2-e1 increases in Fig. 4(b). The sum of HH1-e1 and HH2-e1 basically exhibits a steplike absorption due to a steplike DOS. The same thing occurs for HH2-e2 and HH1-e2, as well as for LH1-e1 and HH3-e1. To make the discussion easier, we use HH-e1 and HH-e2 in this paper to represent the sums

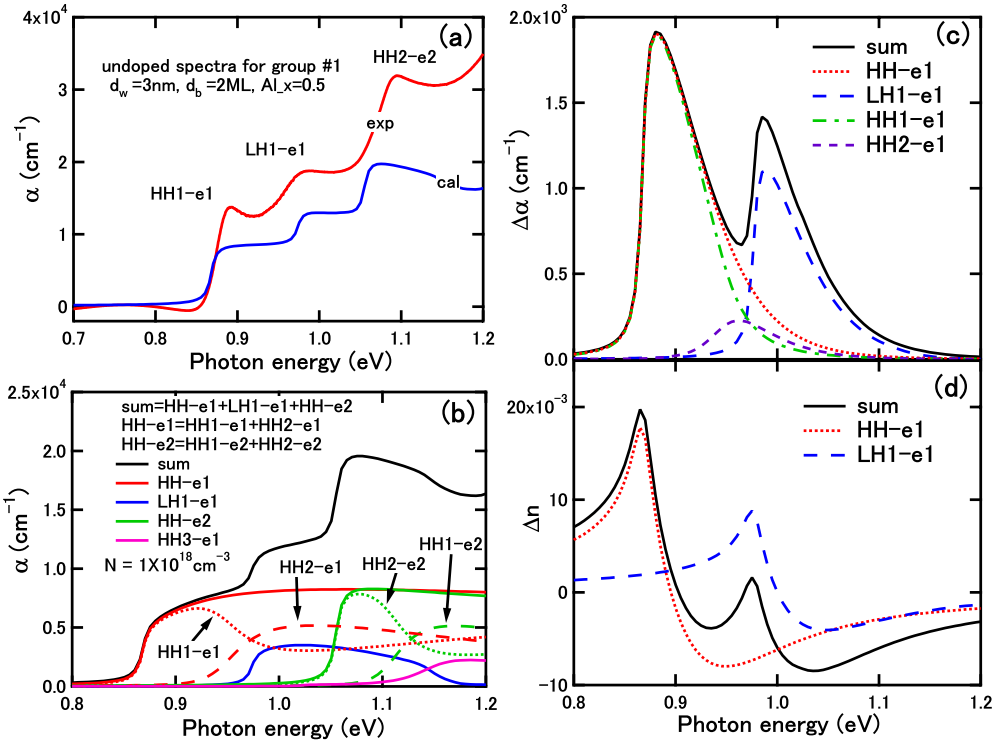

FIG. 4. (Color online) (a) Comparison between the calculated interband absorption spectrum and experimental one measured by FTIR for undoped group 1. (b) Components of the interband absorption spectrum α. The induced absorption $\Delta\alpha$ (c) and index change Δn (d) are shown with their components. In (b)–(d), $N=1\times10^{18}$ cm^{-3}.

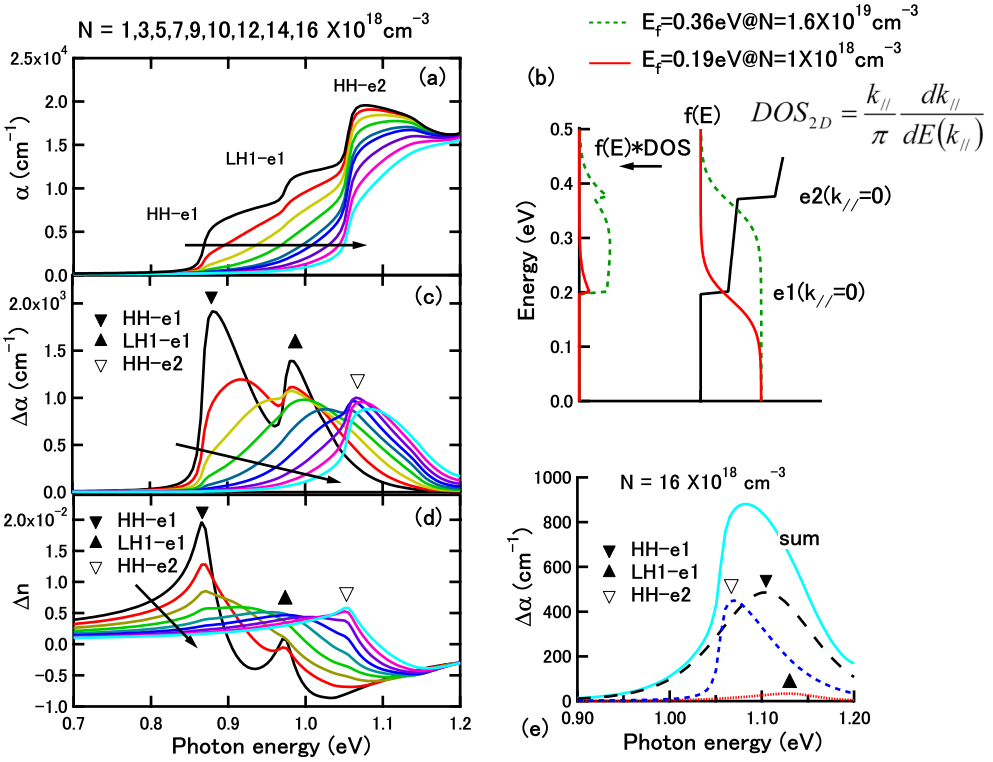

FIG. 5. (Color online) (a) Electron density dependence of interband absorption spectrum α. (b) Schematic figure illustrating the CB Fermi occupation f(e), the nonparabolic two-dimensional DOS numerically calculated from subband dispersions, and their products. Two doping cases $N=1\times10^{18}$, 1.6×10^{19} cm^{-3} are shown. (c) and (d) show $\Delta\alpha$ and Δn, respectively. (e) Components of $\Delta\alpha$ for $N=1.6\times10^{19}$ cm^{-3}. (a)–(e) are calculated for group 1 ($d_w=3$ nm, $d_b=2$ ML, Al_x=0.5).

HH1-e1+HH2-e1 and HH2-e2+HH1-e2, respectively.

Assuming a small carrier depletion $\Delta N=2\times10^{17}$ cm^{-3} by intersubband excitation, we can obtain the induced absorption spectrum $\Delta\alpha$ and index change Δn. In this paper, $\Delta\alpha$ and Δn denote the normalized values $1\times10^{18}\cdot\Delta\alpha/\Delta N$ and $1\times10^{18}\cdot\Delta n/\Delta N$, respectively, for easy comparison between different electron-density regions. Figures 4(c) and 4(d), respectively, show the corresponding $\Delta\alpha$ and Δn for the spectrum in Fig. 4(b). The two peaks (HH1-e1 and LH1-e1) in Figs. 4(c) and 4(d) mainly come from the transitions to e1 because most of the electrons occupy the e1 state at $N=1\times10^{18}$ cm^{-3}. The E_f shift in this case has a negligible influence on the electron occupation at the e2 state because the e2 state is far from E_f. Therefore, induced transitions to the e2 state cannot be observed in Figs. 4(c) and 4(d), which will not always be true if the carrier density is enhanced.

C. Electron-density dependences of α, $\Delta\alpha$, and Δn

Figure 5(a) shows the electron density dependent interband absorption spectra α. To understand Fig. 5(a), Fig. 5(b) schematically demonstrates the CB DOS and Fermi distribution. It is worth mentioning that the two-dimensional DOS is strictly steplike for a parabolic band, while for a nonparabolic one, the steplike DOS is not pure, as depicted in Fig. 5(b), which was numerically calculated from the $k\cdot p$ band dispersions. The energies of two DOS steps correspond to e1 and e2 at $k_{\|}=0$. Two cases of 1×10^{18} and 1.6×10^{19} cm^{-3} for Fermi levels are shown in Fig. 5(b) to illustrate the effect of doping density. With an increase in the electron density from 1×10^{18} to 1.6×10^{19} cm^{-3}, HH-e1 and LH1-e1 shift to higher energy, while HH-e2 remains almost unshifted in Fig. 5(a). The former comes from an increase in k_{Ef} when the electron density is increased. The increase in k_{Ef} also decreases the dipole matrix elements of HH-e1 and LH1-e1, as aforementioned, which accounts for the magnitude decreases for HH-e1 and LH1-e1 absorption. If E_f is shifted upward to a level higher than e1 ($k_{\|}=0$) by several k_BTs (k_B is Boltzmann constant and T is the temperature), the part of the e1 state below E_f is fully occupied by electrons; thus HH-e1 and LH1-e1 occur at $k_{\|}$ much larger than zero with larger transition energies. This explains why the HH-e1 and LH1-e1 steps in Fig. 5(a) gradually vanish with an increase in the electron density. Figure 5(b) demonstrates that e2 ($k_{\|}=0$) is not fully occupied even at 1.6×10^{19} cm^{-3}, which means the HH-e2 transition always occurs near $k_{\|}=0$ for $N<1.6\times10^{19}$ cm^{-3}. Therefore, HH-e2 almost remains unshifted in Fig. 5(a). If the carrier density continues to increase to fully occupy e2 ($k_{\|}=0$), HH-e2 will undergo blueshift and weaken in a way similar to HH-e1.

Figures 5(c) and 5(d) show the variations in $\Delta\alpha$ and Δn with the electron density, respectively. Understanding Figs. 5(c) and 5(d) is straightforward based on Fig. 5(a). Both $\Delta\alpha$ and Δn have two sharp peaks, HH-e1 and LH1-e1 (components not shown), at $N=1\times10^{18}$ cm^{-3}. These two peaks become weak and undergo blueshift for the same reason as was explained for the blueshift in the HH-e1 absorption edge in Fig. 5(a), i.e., the increase in k_{Ef} when an increase in the

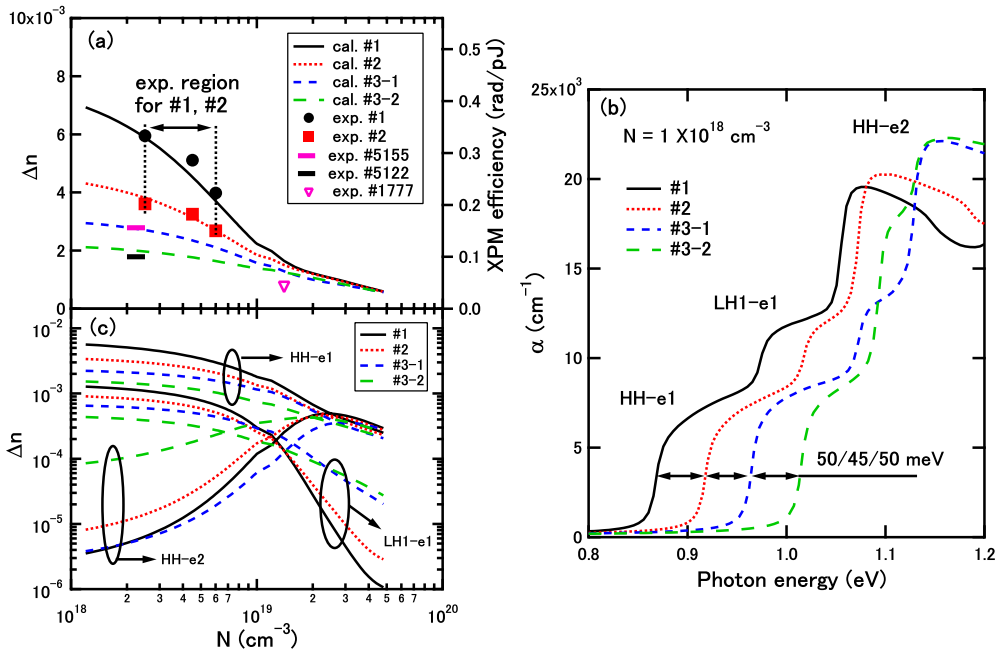

FIG. 6. (Color online) (a) Comparison of the electron density dependence between the calculated index change Δn probed at 0.8 eV and XPM efficiency. No. 5155 and No. 5122 are shown in dashes due to their doping density uncertainty of in Table I. (b) Interband absorption spectra at $N=1\times10^{18}$ cm^{-3} for three groups of CDQWs. No. 1 (d_w=3 nm, d_b=2 ML, Al_x=0.5), No. 2 (d_w=2.9 nm, d_b=3 ML, Al_x=0.5), No. 3–1 (d_w=2.6 nm, d_b=2 ML, Al_x=1), No. 3–2 (d_w=2.6 nm, d_b=4 ML, Al_x=1) (c) components of (a).

electron density. The HH-e2 component gradually dominates both $\Delta\alpha$ and Δn with the enhancement in electron occupation at the e2 state. Figure 5(e) show the components for $\Delta\alpha$ at $N=1.6\times10^{19}$ cm^{-3}. Under this density, e1 ($k_{\|}=0$) has been fully occupied, however, e2 ($k_{\|}=0$) has not been yet, as seen in Fig. 5(b). Thus the HH-e1 transition occurs at $k_{\|}$ much larger than zero, but HH-e2 occurs near $k_{\|}=0$ due to the partial occupation at e2 ($k_{\|}=0$). This explains their spectral difference in symmetry in Fig. 5(e) and why the blueshift is not clearly observed for HH-e2 in Figs. 5(c) and 5(d). $\Delta\alpha$ in Fig. 5(c) is no longer a simple Lorentz function due to the overall contributions from several transitions. Similarly, Δn in Fig. 5(d) exhibits a complicated photon energy dependence that varies with carrier density. Focusing on the lower energy side of the absorption edge, Δn increases when tuning the photon energy close to the absorption edge. This feature is more prominent at a low doping level.

D. Calculation vs experiment for electron-density dependences of Δn at 0.8 eV

Considering the application at 1.55 μm (close to our probe wavelength of 1541 nm), we extracted the index change values at 0.8 eV from Fig. 5(d) and plotted these values as a function of the electron density in Fig. 6(a). Figure 6(a) compares the calculated index change with the experimental XPM efficiency for three groups. The Δn and XPM efficiency axes were aligned using No. 645 which has the highest XPM efficiency (0.33 rad/pJ). The dependence of the experimental XPM efficiency on the electron density well follows that of the calculated index change, especially for groups 1 and 2.

To clarify the XPM difference in the low electron-density region for three groups of CDQWs, the calculated interband absorption spectra are shown in Fig. 6(b) to display their absorption edge differences. The smaller interband absorption edge the group has in Fig. 6(b), the higher is its index change in Fig. 6(a). The 50 meV difference in HH1-e1 between No. 1 and No. 2 matches the experimental absorption edge separation between No. 645 and No. 649 in Fig. 2(d). For the three groups in Fig. 6(b), the important parameters that greatly influence the absorption edge are the barrier composition and thickness. An $Al_{0.5}Ga_{0.5}As$ barrier gives a lower absorption edge than an AlAs one and a thinner barrier gives a lower absorption edge than a thicker one. This is because $Al_{0.5}Ga_{0.5}As$ has a smaller band offset for the well than AlAs and a thinner barrier has stronger interwell coupling, both of which shift the e1 state to a lower energy and the HH1 to a higher energy. Therefore, for equal electron densities, groups 1 and 2 have larger index changes than No. 3–1 and No. 3–2. Meanwhile, No. 1 is larger than No. 2, and No. 3–1 is larger than No. 3–2. This explains the experimental facts that No. 1 had a larger XPM efficiency than No. 2 for equally doped samples and No. 5155 had larger XPM efficiency than No. 5122, as shown in Fig. 6(a). No. 1777 had the lowest XPM efficiency due to its high doping density and thicker AlAs barrier.

The index change probed at 0.8 eV in Fig. 6(a) is the sum of the components in Fig. 6(c), where the HH-e1 and LH1-e1 contributions decrease, whereas the HH-e2 contribution first increases and then decreases as the electron density is enhanced. The former results from the blueshift of the absorption edge and the decrease in the dipole matrix element [Fig. 3(b)] with the increase in k_{Ef}. To explain the latter, the electron occupation should be considered further. If e2 ($k_{\|}=0$) is

not fully occupied, the induced absorption always occurs at $k_{\|}=0$ for HH-e2. Under this situation, the induced absorption strength depends on the electron occupation at e2 ($k_{\|}=0$). In other words, the HH-e2 contribution will increase when more and more electrons occupy the e2 ($k_{\|}=0$). However, once the e2 ($k_{\|}=0$) is fully occupied, HH-e2 will decrease for the same reason as HH-e1. Therefore, we observe a maximum for HH-e2 in Fig. 6(c). The HH-e1 and LH1-e1 contributions decrease with almost equal speed with an increase in N in the low-density region ($<6\times10^{18}$ cm^{-3}) because they share a common final state of e1. However, when $N>1\times10^{19}$ cm^{-3}, the LH1-e1 contribution decreases much faster than HH-e1 due to its dramatic reduction in the dipole matrix element, as seen in Fig. 3(b).

In the low-density region, No. 1>No. 2>No. 3−1>No. 3−2 for the HH-e1 and LH1-e1 contributions because of their increasing absorption edge order, as seen in Fig. 6(b). For the HH-e2 contribution, the energy separation between e1 and e2 is determinative. If a CDQW has a larger |e1-e2|, its e2 state has lower electron occupation because it is farther from E_f for equal doping. Therefore, this CDQW has a smaller HH-e2 contribution. No. 3−2<No. 2<No. 1, No. 3–1 in the e1-e2 energy separation in Fig. 6(b), such that No. 3–2 and No. 2 are larger than No. 1 and No. 3–1 in the HH-e2 contribution for low electron density, as shown in Fig. 6(c). The e1-e2 energy separation depends on the coupling strength between two wells, since e1 and e2 gradually separate when the coupling becomes stronger with a decrease in the barrier thickness.

E. Dependence of XPM efficiency on interband absorption edge

An important feature in our model described in Sec. III is that the XPM efficiency at a specific photon energy will decrease when the interband absorption edge moves away from this probe photon energy. Therefore, we compare the absorption edge dependences between the experimental XPM efficiency and the calculated index change for all samples in Fig. 7. The experimental absorption edge is approximately regarded as the photon energy at an absorption coefficient =200 cm^{-1} in Fig. 2(d), while the calculated absorption edge is from the electron density dependent absorption spectra such as those in Fig. 5(a). As shown in Fig. 7, the XPM efficiencies for all samples almost follow the same reciprocal dependence on the interband absorption edge. Such a sample-independent reciprocal function is well reproduced by the calculated index change. The differences in the absorption edge in Fig. 6(b) are also plotted in Fig. 7 to clearly trace the different groups. When the absorption edge is tuned close to the probe photon energy (0.8 eV), the XPM efficiency as well as the index change are greatly enhanced, and meanwhile the enhancement speed of the index change increases. This explains why the XPM efficiency of No. 1 decreases faster than No. 2 in Fig. 6(a) with increasing the electron density. If the interband absorption edge is far enough away from 0.8 eV in Fig. 7, different CDQWs tend to be identical. This accounts for the disappearance in the difference between different CDQW structures for high electron density in Fig. 6(a). Therefore, the electron density dependences of the calculated index change and the experimental XPM efficiency can be well understood by Fig. 7, where the energy separation between the interband absorption edge and the probe photon energy is the dominant factor.

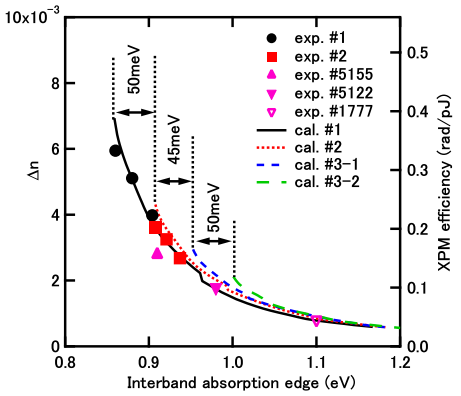

FIG. 7. (Color online) Dependences on the interband absorption edge for both the calculated index change Δn probed at 0.8 eV and the experimental XPM efficiency. The interband absorption edge in the calculation is from the interband absorption spectra under different electron densities and the experimental one was extracted from Fig. 2(d) at $\alpha_{WG}=200$ cm^{-1}. The interband absorption edge differences between different groups in Fig. 6(b) are also shown. The calculated CDQW structures are given in Fig. 6.

V. OPTIMIZATION OF QUANTUM WELL STRUCTURE

Up to now, the experimental results for two groups of CDQWs with $Al_{0.5}Ga_{0.5}As$ coupling barriers and the reason why $Al_{0.5}Ga_{0.5}As$ gives a larger XPM efficiency than AlAs have been well interpreted by our $k\cdot p$ calculations. Therefore, we can further tailor the CDQW structure with the intention of enhancing XPM efficiency. The primary goal is tuning both HH1-e1 and LH1-e1 absorption edges to 0.8 eV to enhance their contributions, while keeping the intersubband transition e1-e4 as close to 0.8 eV as possible. Our idea is to weaken the confinement in CB and VB by decreasing the band offset of the AlGaAs coupling barrier through decreasing the Al composition so that e1 will undergo downshift and both the HH and LH bands will shift upward. For the CDQW structure of No. 1, Fig. 8(a) plots the calculated the transition energies at $k_{\|}=0$ versus the Al composition. As expected, HH1-e1 and LH1-e1 are both shifted to low energy, while e1-e4 is slightly shifted to high energy because e1 decreases faster than e4 when CBO is reduced by the decrease in the Al composition. The adjustment in Al composition from 0.5 to zero results in ~70 meV decreases for both HH1-e1 and LH1-e1, and a ~50 meV increase from 0.78 to 0.83eV for e1-e4. Therefore, the XPM efficiency will be enhanced if we reduce the Al composition of the AlGaAs coupling layer.

To examine this expectation, we calculated the electron density dependence of the index change at 0.8 eV using the No. 1 CDQW under different Al compositions, as shown in Fig. 8(b). As was discussed, heavy doping has a negative effect for our purpose. Thus, we concentrate on a low doping

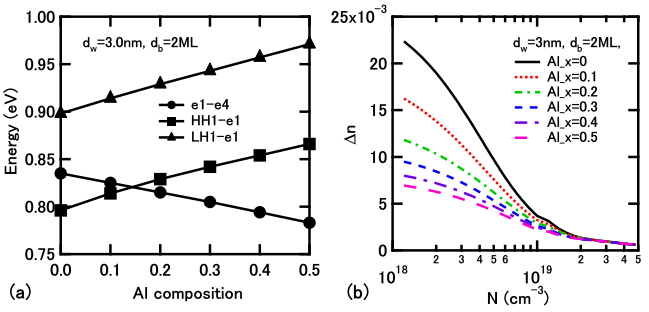

FIG. 8. (Color online) (a) Transition energies ($k_{\|}$=0) of e1-e4, HH1-e1, and LH1-e1 versus Al composition of the coupling barrier for d_w=3 nm and d_b=2 ML. (b) Calculated electron density dependence of the index change at 0.8 eV for different Al compositions.

density ($1\sim4\times10^{18}$ cm^{-3}). In this region, the index change increases with decreasing Al composition. For $N\sim1\times10^{18}$ cm^{-3}, an approximately threefold enhancement in Δn is obtained when the Al composition is decreased from 0.5 to zero. Even when N is increased to 4×10^{18} cm^{-3}, there is a twofold enhancement. Such a large enhancement comes from the redshifts of the absorption edges for both the HH1-e1 and LH1-e1 transitions, as shown in Fig. 8(a).

VI. CONCLUSIONS

In this study, we systematically investigated the XPM in InGaAs/AlAsSb CDQW systems with AlGaAs as the coupling barrier from both the experimental and calculation sides. The experimental results were quantitatively explained by a refined interband dispersion model under intersubband excitation based on eight-band $k\cdot p$ calculation. The calculated index change at 1.55 μm and the experimental XPM efficiency both exhibited a reciprocal dependence on the interband absorption edge, which agreed well with each other. Therefore, it is the blueshift of the interband absorption edge that mainly results in a decrease in the XPM efficiency when increasing the doping density. Decreasing the Al composition from 0.5 to zero in AlGaAs coupling barrier could enhance the contributions from both HH and LH. A threefold enhancement in XPM efficiency is expected for a doping density of $\sim1\times10^{18}$ cm^{-3}.

ACKNOWLEDGMENTS

This work was partly supported by the New Energy and Industrial Technology Development Organization (NEDO). G.W. Cong also acknowledges support from the Japan Society for the Promotion of Science.

*gw-cong@aist.go.jp
†r-akimoto@aist.go.jp

[1] D. Cotter, R. J. Manning, K. J. Blow, A. D. Ellis, A. E. Kelly, D. Nesset, D. Phillips, A. J. Poustie, and D. C. Rogers, Science **286**, 1523 (1999).
[2] H. C. Liu and F. Capasso, *Intersubband Transitions in Quantum Wells: Physics and Device Applications II* (Academic Press, New York, 2000), Chap. 1.
[3] H. Tsuchida, T. Simoyama, H. Ishikawa, T. Mozume, and M. Nagase, Opt. Lett. **32**, 751 (2007).
[4] R. Akimoto, T. Simoyama, H. Tsuchida, S. Namiki, C. G. Lim, M. Nagase, T. Mozume, T. Hasama, and H. Ishikawa, Appl. Phys. Lett. **91**, 221115 (2007).
[5] R. Akimoto, G. W. Cong, M. Nagase, T. Mozume, H. Tsuchida, H. Ishikawa, and T. Hasama, *Proceedings of the 34th European Conference and Exhibition on Optical Communication* (IEEE, Brussels, Belgium, 2008), Vol. 5, p. 57.
[6] G. W. Cong, R. Akimoto, M. Nagase, T. Mozume, T. Hasama, and H. Ishikawa, Phys. Rev. B **78**, 075308 (2008).
[7] S. L. Chuang and D. Ahn, J. Appl. Phys. **65**, 2822 (1989).
[8] S. L. Chuang, *Physics of Optoelectronic Devices* (Wiley-Interscience, New York, 1995), Chap. 9.
[9] S. Gozu, T. Mozume, R. Akimoto, K. Akita, G. W. Cong, and H. Ishikawa, Appl. Phys. Express **2**, 042201 (2009).
[10] M. Nagase, R. Akimoto, T. Simoyama, G. W. Cong, T. Mozume, T. Hasama, and H. Ishikawa, IEEE Photon. Technol. Lett. **20**, 2183 (2008).
[11] T. B. Bahder, Phys. Rev. B **41**, 11992 (1990); **46**, 9913 (1992).
[12] G. Liu and S. L. Chuang, Phys. Rev. B **65**, 165220 (2002).
[13] W. W. Chow and S. W. Koch, *Semiconductor-Laser Fundamentals: Physics of the Gain Materials* (Springer, New York, 1999), Chap. 6.
[14] A. V. Gopal, H. Yoshida, T. Simoyama, J. Kasai, T. Mozume, and H. Ishikawa, Appl. Phys. Lett. **83**, 1854 (2003).
[15] D. G. Revin, L. R. Wilson, E. A. Zibik, R. P. Green, J. W. Cockburn, M. J. Steer, R. J. Airey, and M. Hopkinson, Appl. Phys. Lett. **84**, 1447 (2004).
[16] N. Georgiev and T. Mozume, J. Appl. Phys. **89**, 1064 (2001).
[17] T. Mozume, J. Kasai, M. Nagase, T. Simoyama, and H. Ishikawa, J. Cryst. Growth **301-302**, 177 (2007).
[18] M. Sugawara, N. Okazaki, T. Fujii, and S. Yamazaki, Phys. Rev. B **48**, 8102 (1993).
[19] I. Vurgaftman, J. R. Meyer, and L. R. Ram-Mohan, J. Appl. Phys. **89**, 5815 (2001).